How to cite: *Angew. Chem. Int. Ed.* **2023**, *62*, e202304293
doi.org/10.1002/anie.202304293

Electrochemistry

Anodic and Cathodic Platinum Dissolution Processes Involve Different Oxide Species

*Timo Fuchs, Valentín Briega-Martos, Jakub Drnec, Natalie Stubb, Isaac Martens, Federico Calle-Vallejo, David A. Harrington, Serhiy Cherevko, and Olaf M. Magnussen**

Abstract: The degradation of Pt-containing oxygen reduction catalysts for fuel cell applications is strongly linked to the electrochemical surface oxidation and reduction of Pt. Here, we study the surface restructuring and Pt dissolution mechanisms during oxidation/reduction for the case of Pt(100) in 0.1 M $HClO_4$ by combining *operando* high-energy surface X-ray diffraction, online mass spectrometry, and density functional theory. Our atomic-scale structural studies reveal that anodic dissolution, detected during oxidation, and cathodic dissolution, observed during the subsequent reduction, are linked to two different oxide phases. Anodic dissolution occurs predominantly during nucleation and growth of the first, stripe-like oxide. Cathodic dissolution is linked to a second, amorphous Pt oxide phase that resembles bulk PtO_2 and starts to grow when the coverage of the stripe-like oxide saturates. In addition, we find the amount of surface restructuring after an oxidation/reduction cycle to be potential-independent after the stripe-like oxide has reached its saturation coverage.

Introduction

For the transition to a sustainable society, the polymer electrolyte membrane fuel cell (PEMFC) provides a way to convert renewable energy of sun and wind stored in hydrogen and other fuels into electrical energy. However, the wide-spread adoption of the PEMFC is still mainly hampered by its cost and the lack of durability of the fuel cell components.[1,2] A primary degradation mechanism of the fuel cell is the dissolution of the platinum-based electrocatalyst at the fuel cell cathode, which occurs if the electrode is subjected to potentials where the Pt is oxidized.[3–11] This causes Pt mass loss and other secondary degradation of the catalyst, such as Ostwald ripening of the platinum nanoparticles, which lowers the electrochemically active surface area.[3,12–14] To compensate this loss, a surplus of Pt catalyst loading at the fuel cell cathode is required to achieve a sufficient life-time of the fuel cell, which increases its cost.[2] On the other hand, understanding Pt dissolution on the atomic scale and the resulting knowledge-driven design of more advanced electrocatalysts and/or optimization of fuel cell operation parameters can potentially lead to stable fuel cells with low Pt loading. Hence, considerable research efforts have been dedicated towards understanding the complex interplay between platinum oxidation and dissolution.

Time-resolved on-line inductively coupled plasma mass spectrometry (on-line ICP-MS) Pt dissolution measurements have revealed that Pt dissolution is a transient process which coincides not only with Pt oxide formation but also subsequent reduction[3–5,15] of the formed oxide. It has also been shown that Pt can dissolve from Pt oxide during periods at open circuit, which the authors attribute to a purely chemically driven dissolution mechanism.[16] The dissolution that takes place during Pt oxidation, commonly denoted as "anodic dissolution", is a potential-dependent process, showing an initial increase of dissolution rate followed by a decrease caused by surface passivation with

[*] T. Fuchs, Prof. O. M. Magnussen
Institut für Experimentelle und Angewandte Physik,
Christian-Albrechts-Universität zu Kiel,
Olshausenstr. 40, 24098 Kiel, Germany
E-mail: magnussen@email.uni-kiel.de

V. Briega-Martos, S. Cherevko
Forschungszentrum Jülich GmbH, Helmholtz-Institute Erlangen-Nürnberg for Renewable Energy (IEK-11),
Cauerstr. 1, 91058 Erlangen, Germany

J. Drnec, I. Martens
Experimental division, European Synchrotron Radiation Facility,
71 Avenue des Martyrs, 38000 Grenoble, France

N. Stubb, Prof. D. A. Harrington
Chemistry Department, University of Victoria,
Victoria, British Columbia, V8W 2Y2, Canada

F. Calle-Vallejo
Nano-Bio Spectroscopy Group and European Theoretical Spectroscopy Facility (ETSF), Department of Advanced Materials and Polymers: Physics, Chemistry and Technology, University of the Basque Country UPV/EHU,
Av. Tolosa 72, 20018 San Sebastián, Spain
and
IKERBASQUE, Basque Foundation for Science,
Plaza de Euskadi 5, 48009 Bilbao, Spain

stable oxide.[4] For the platinum dissolution during oxide reduction ("cathodic dissolution"), a linear correlation of dissolved platinum with the cathodic electrochemical charge transfer during oxide reduction (usually equated to the amount of formed oxide) was found.[17] To explain this behavior, different Pt dissolution mechanisms based on the thermodynamics of bulk Pt and Pt bulk oxide materials have been proposed, which lead to Pt dissolution in form of either Pt^{2+} or Pt^{4+} ions in the electrolyte solution.[8,9,11] These ions were attributed by Wang et al. to dissolution of PtO and PtO_2, respectively,[11] but this assignment was not unequivocally shared by other groups.[8–10] Overall, the detailed Pt dissolution mechanisms are still strongly under debate. Specifically, explanations on the basis of the thermodynamics of bulk Pt and its oxides are problematic, because in the operational range of fuel cells only the Pt surface atoms are oxidized, resulting in ultrathin surface oxide with strongly different structures from those of bulk Pt oxides. A true understanding of the Pt dissolution mechanism therefore requires a more detailed atomic-scale description.

Platinum surface oxidation has been a model system to study the electrochemical oxidation of metals and numerous models have been proposed for this process. Early works described Pt surface oxidation by the so-called place-exchange, where adsorbed oxygen species exchange their lattice site with the underlying Pt atoms.[18,19] In situ studies by modern surface-sensitive methods combined with density functional theory (DFT) calculations provided a more detailed picture and revealed that differences in the atomic-scale structure of Pt surface oxides on different single crystal surfaces can explain the different susceptibility of the platinum oxide to dissolve during its formation.[20–25] Specifically, our group previously reported results by surface X-ray diffraction (SXRD), ICP-MS, and DFT calculations on the initial stages of Pt(111) and Pt(100) oxidation, that suggested a direct link between the surface oxide structure, Pt dissolution, and irreversible Pt surface restructuring.[23] There, we demonstrated that the higher stability of Pt(111) is caused by differences in the oxide structure rather than a higher onset potential for oxidation: While the extracted Pt atoms on Pt(111) occupy a position directly above the original surface lattice site,[23,26–28] in the case of Pt(100) they reside on a bridge position over two vacancy sites, forming oxide stripes.[23]

This scenario provides a good description of the initial stages of electrooxidation up to approximately 1.15 V, where the oxide coverage is low, but fails at higher oxide coverage. At higher potentials, SXRD studies indicate an increasing disorder, which up to now has impeded a more detailed analysis of the oxide structure.[27,29] Spectroscopic measurements indicate that at least two types of platinum oxides are formed in this range. In X-ray photoelectron spectroscopy studies of platinum surfaces and nanoparticles these oxide phases were assigned to different oxidation states of up to Pt^{4+}.[30–32] Measurements on Pt(111) and Pt(100) single crystals by in situ surface-enhanced Raman spectroscopy reported frequency shifts, that were attributed to the formation of platinum (su)peroxide or amorphous PtO_2.[33] The consequences of multiple surface oxide phases for the Pt dissolution behavior are unclear, however. Specifically, none of these previous experimental studies, including our previous work on the very initial stages of Pt(100) oxidation,[23] addressed the mechanistic differences between anodic and cathodic Pt dissolution. How the latter is influenced by the atomic-scale structure of the surface oxide was up to now only explored in recent DFT calculations.[24]

In this study, we investigate the structure of the electrochemically formed surface oxide on Pt(100) in 0.1 M $HClO_4$ and 0.1 M H_2SO_4 at potentials higher than 1.1 V. We verify the presence of a second oxide phase, provide details on its atomic-scale structure, and determine the coverage of both oxide phases as a function of potential. This analysis is challenging due to the need to determine two coexisting surface structures that exhibit disorder, which has not been attempted before for an electrochemical interface. Key for performing these detailed structural studies was the use of in situ high energy surface X-ray diffraction (HESXRD).[34] This emerging method allows rapid measurements of a large volume of the reciprocal space, which was a requirement for the reliable quantitative determination of such complex multi-phase structures. Comparison of the potential-dependent coverage of the two Pt surface oxide phases with ICP-MS data obtained under identical conditions allows direct quantitative correlation of the anodic and cathodic Pt dissolution with the complex surface structure and reveals that anodic and cathodic dissolution can be attributed to different Pt oxides.

After reduction of the surface oxide, pronounced surface roughening can be observed,[21,29,35–37] which makes the use of shape-controlled catalysts in fuel cells challenging. We additionally determine the coverage of surface defects as number of adatoms and vacancies after reduction, which allows correlation of the two Pt oxide phases with the irreversible surface roughening.

Results and Discussion

Influence of electrolyte on the oxidation behavior of Pt(100)

The surface oxidation of Pt(100) in perchloric and sulfuric acid solution was initially characterized by combined cyclic voltammograms and X-ray intensity measurements (Figure 1). Here, the X-ray intensity was recorded near the anti-Bragg position of a Pt crystal truncation rod (CTR), where it is highly sensitive to oxide formation.[23,26,38,39] The obtained CVs are in good agreement with those recorded in the literature.[40–42] Starting from the negative potential limit, they first exhibit the hydrogen adsorption region which overlaps above about 0.35 V with a region associated with anion adsorption/desorption.[43] The OH adsorption in perchloric acid electrolyte occurs in a broad region around 0.5 V while the (bi)sulfate adsorption in sulfuric acid electrolyte manifests as a peak at 0.4 V. Finally, at around 1.0 V, an anodic current peak is observed that is generally attributed to the oxidation of adsorbed OH to adsorbed oxygen.[33,40,44] In our previous study,[23] we showed that in 0.1 M $HClO_4$ the onset of Pt(100) oxidation manifests as a sharp drop in

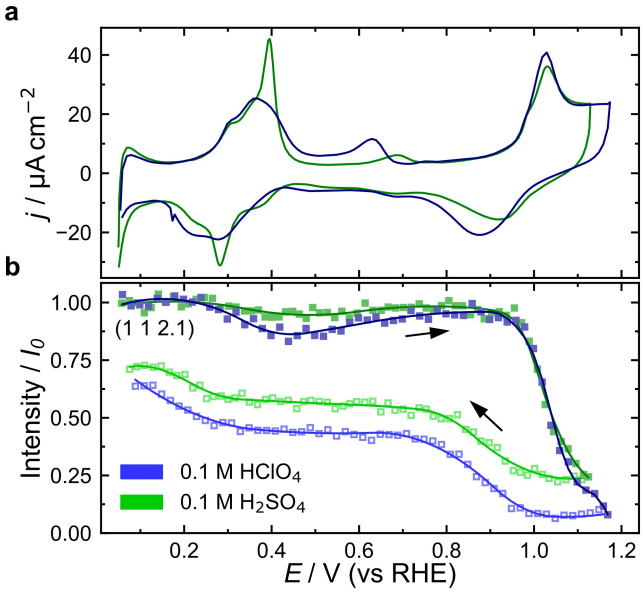

Figure 1. Oxidation and reduction in 0.1 M H_2SO_4 and 0.1 M $HClO_4$ electrolyte. a) Cyclic voltammograms and b) corresponding X-ray intensity at (1 1 2.1) in 0.1 M H_2SO_4 and 0.1 M $HClO_4$. The electrochemical and structural data were simultaneously recorded at 20 mV/s and indicate that formation of the surface oxide above 0.98 V proceeds in an identical manner. The solid lines in b) serve as a guide to the eye. The data in 0.1 M $HClO_4$ has been published previously in Ref. [23].

X-ray intensity, which coincides with this current peak. The X-ray intensity does not fully recover on the sweep back in negative direction, indicating that the oxide reduction results in irreversible structural changes of the Pt surface. An identical behavior is found in sulfuric acid solution (Figure 1, green). In particular, the decay of the intensity in the surface oxidation regime is virtually indistinguishable to that in $HClO_4$ and the intensity recovers only partially during oxide reduction, with the same potential dependence as in $HClO_4$ (the offset in intensity as compared to that in $HClO_4$ is related to the less positive upper potential limit of the CV and the corresponding difference in oxide surface coverage). Furthermore, the detailed surface crystallographic studies presented in the following section show that the oxidized Pt surface can be described in both electrolytes by the same structural model. We therefore conclude that under these conditions the electrolyte has no major influence on the Pt(100) surface oxide structure and its initial formation kinetics. However, we cannot rule out a weak influence of the anion species on the slower oxidation kinetics which occurs on the timescale of minutes after the initial fast oxidation.[26,45,46] The influence of both electrolyte solutions on Pt dissolution has been compared on polycrystalline Pt samples.[47,48] No or negligible influence of the anion species in the electrolyte was found. Although an influence cannot be ruled out for single crystal samples without an explicit experiment, these results suggest that the influence of these anion species on Pt dissolution is weak.

Structure of the Pt(100) oxide

The atomic-scale oxide structure of Pt(100) in the initial stages of oxidation up to 1.17 V has been previously determined using a combination of CTR analysis and DFT calculations.[23] These studies revealed that the extracted Pt atoms in the oxide are located about 1.4 Å above the plane of the Pt(100) surface atoms and are shifted sideways by half an Pt–Pt bond length, i.e., they reside at a bridge site position with respect to the surface lattice. Due to this lateral shift, it is unlikely that the extracted Pt atoms are distributed on the surface as isolated extracted Pt atoms on top of a single vacancy. In the latter case, the distance to the closest Pt surface atoms would be just 1.97 Å, which is well below the bond length of 2.77 Å in bulk Pt. The extracted Pt atoms therefore have to reside in the center of a double vacancy. According to the DFT calculations in Ref. [23], they are stabilized in this position by surrounding adsorbed oxygen in a square-planar configuration. This geometry favors the growth of Pt oxide stripes, consisting of consecutive extracted Pt atoms along the [011] or [0$\bar{1}$1] directions (see Figure 2a, left hand side). The theoretical maximum coverage of extracted Pt atoms in the stripe oxide is 0.5 ML, which corresponds to a surface where every second Pt atom row is extracted. According to our previous study, this coverage is already approached at a potential of 1.12 V. However, electrochemical and spectroscopic measurements clearly indicated continuation of surface oxidation at higher potentials.[33,40,44] To account for this, the stripe oxide model must be extended to describe the oxidized surface at higher potentials.

To clarify the potential-dependent surface oxide structure from the initial stripe oxide growth regime up to the onset of oxygen evolution we performed in situ HESXRD studies in 0.1 M H_2SO_4, in which we recorded six symmetrically non-equivalent non-specular CTRs as well as the specular CTR at 12 potentials between 0.93 V and 1.63 V. The very large reciprocal space volume covered in these HESXRD measurements as well as the inclusion of the specular CTR was decisive for a reliable determination of the complex, highly disordered Pt oxide structure. Figure 2b shows selected CTRs of an experiment, where the oxide was formed by gradually increasing the potential in steps of first 50 and then 100 mV (the full CTR sets are provided in Figure S1). To account for the slow kinetics of oxide growth, the CTR acquisition started five minutes after the potential was applied. Detailed kinetic measurements revealed that after this time the oxide structure was stable on the time scale required for acquiring the CTR data (25 min). In-depth modeling of the obtained CTR data revealed that the HESXRD results could not be properly described by the stripe oxide phase alone. Although the non-specular CTRs are in good agreement with the data up to 1.62 V, showing that the part of the oxide that is commensurate to the Pt lattice is well described by the stripe oxide model, the specular CTR fits exhibit systematic deviations at higher potentials. This indicates the presence of a second oxide phase with pronounced lateral disorder. We considered in our analysis a number of different surface oxide models

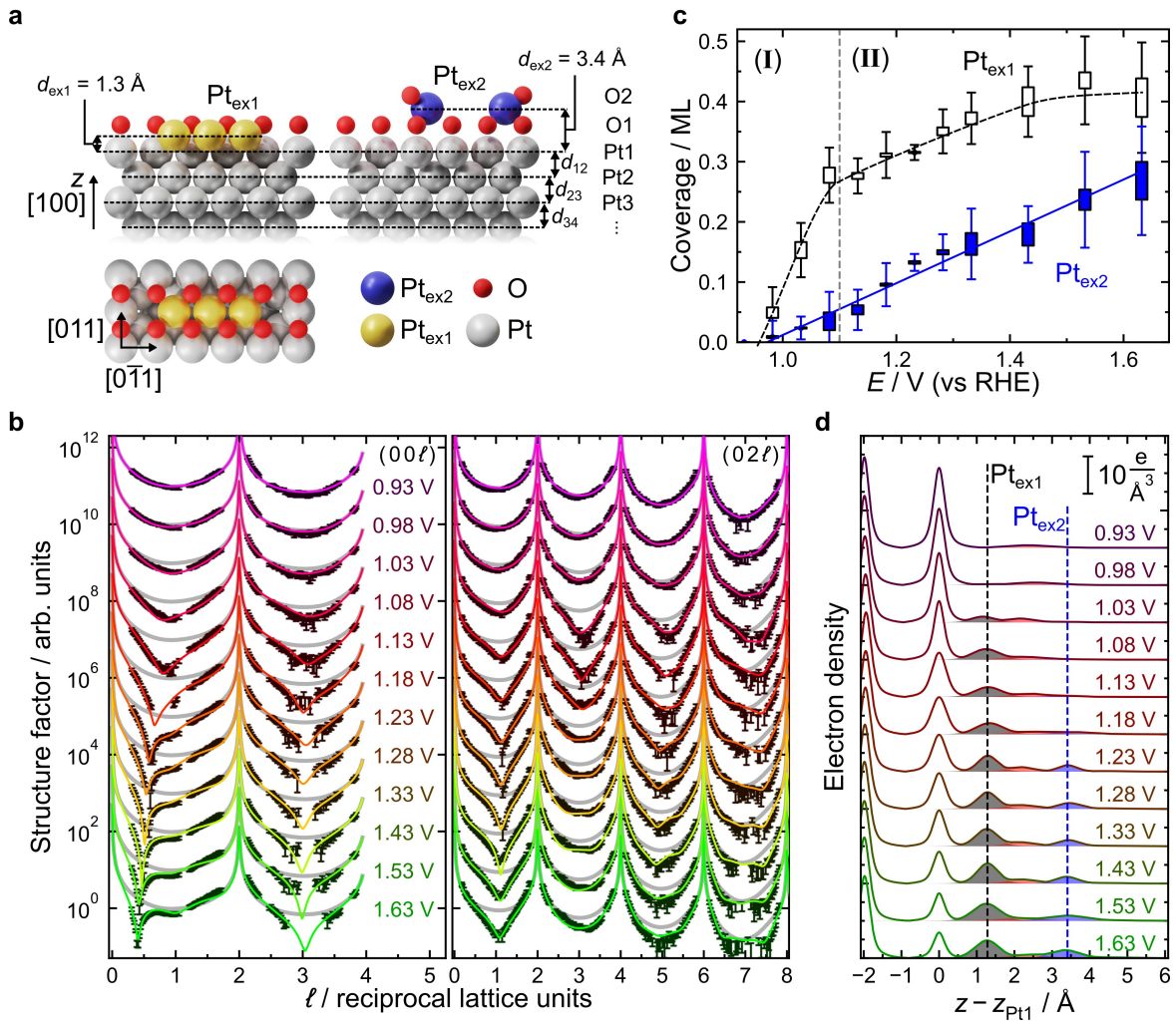

Figure 2. Atomic-scale structure of the stripe-like and amorphous oxide phases. a) Schematic illustrations of the two Pt oxide phases. On the left, top and side views of the geometry of the Pt_{ex1} in the stripe oxide are shown; the right side provides a side view of the Pt_{ex2} extraction site. Arrows indicate fitted vertical distances (d) between interface species. All other fit parameters and the best-fit parameter values are summarized in Table S2. b) Specular CTR (00ℓ) and one of the six measured non-specular, non symmetrically equivalent CTRs at potentials from close to the onset of oxidation at about 1 V up to 1.63 V. The CTR data at each potential are offset by a factor of 8 with respect to each other and are shown together with fits (colored solid lines). As a reference, the CTR fit of the data close to the onset of oxidation at 0.93 V is shown as solid gray lines. The full set of the measured CTRs and the corresponding fits are shown in Figure S1. c) Potential-dependent coverage of the extracted Pt atoms in Pt_{ex1} sites and Pt_{ex2} sites. The stripe oxide and amorphous oxide growth regimes are marked with (**I**) and (**II**), respectively. Rectangular boxes indicate the systematic error caused by the ambiguity of the location of the O_{ad} layer. The error bars represent the standard uncertainties of the CTR fits as standard deviations. Further details on the error analysis are given in the Supporting Information. d) Electron density profiles along the surface normal corresponding to the CTR fits. The density profiles at different potentials are offset from each other by 10 e Å^{-3}. Black and blue dashed vertical lines indicate the location of the Pt_{ex1} and Pt_{ex2} extraction site, respectively.

(Figure S2), which were evaluated by jointly fitting them to all CTRs at each potential (see the Supporting Information for the fitting procedures and a detailed discussion of all considered models). The best description was obtained by coexistence of the stripe oxide with a second oxide phase, in which the Pt atoms resided above the stripe oxide. Illustrations of the resulting geometries of these surface oxide phases are shown in Figure 2a. Here and in the following, the Pt atoms in the stripe oxide are denoted as Pt_{ex1} and the Pt atoms in the oxide above it are referred to as Pt_{ex2}.

This surface oxide model provides a good fit of all measured CTRs if the Pt_{ex2} are placed at a potential-independent vertical distance of $d_{ex2} = 3.4 \pm 0.3$ Å from the surface (the given error includes the deviation of the obtained d_{ex2} value from the CTR fits at all potentials as well as the statistical error of each individual CTR fit). Except for the coverages of the two oxide species, which increase with potential, the structural parameters remain similar at all potentials (see the Supporting Information for a detailed description of all fitted structural parameters, the fit error estimation, and their respective values). The absence of lateral order in the second oxide phase is supported by the

detailed CTR analysis as well as the lack of in-plane diffraction peaks corresponding to a two-dimensional ordered oxide layer (see Figure S4). The large vertical distance of the Pt_{ex2} from the surface suggest that it is stabilized by additional oxygen species. Also DFT calculations, which will be discussed below, suggest the presence of oxygen species above the Pt_{ex2}. However, its presence could not be verified unambiguously with the CTR analysis due to the weak scattering by these oxygen species. Nevertheless for the CTR fits, we tentatively placed oxygen atoms at a vertical distance of 1.1 Å relative to the Pt_{ex2}. This distance corresponds to the spacings in a surface O–Pt–O layer of α-PtO_2(0001), which was observed in gas-phase oxidation of Pt(111),[49,50] and is close to the vertical distances in PtO_2– or Pt_3O_4– like bulk oxides[51,52] (see Figure S3 and Table S1). This model leads to minor improvements in the fit of the specular CTR as compared to models without oxygen (Figure S2). Depending on the inclusion of oxygen and on their locations, the Pt_{ex1} and Pt_{ex2} coverages obtained from the model exhibit small differences on the order of a few percent. With increasing potential, the surface is further oxidized, which manifests in a continuous increase of the coverage of both Pt_{ex1} and Pt_{ex2} (Figure 2c). However, the coverages of the two species do not grow with equal rates. Instead, two distinctly different regimes are found. In the initial stages of oxidation up to about 1.1 V (region **I**), predominant growth of the stripe oxide occurs, until a Pt_{ex1} coverage of about 0.3 ML is reached. The Pt_{ex2} coverage remains in this region below 0.05 ML, i.e., the amorphous oxide Pt_{ex2} is at most present as a minority species. At potentials higher than 1.1 V (region **II**), the potential-dependent change in Pt_{ex1} coverage substantially decreases until a saturation coverage between 0.40 and 0.45 ML is reached above 1.4 V. Taking into account that a perfectly defect-free stripe oxide phase would correspond to 0.5 ML of Pt_{ex1}, a saturation of the Pt_{ex1} coverage in this range is expected. A similar saturation coverage was also observed in other SXRD experiments (see below). The coverage of the second, amorphous oxide species Pt_{ex2} increases linearly with potential at 0.43 ± 0.07 ML/V over the complete potential range. Within the experimental errors, it is close to zero in region **I**, which explains why the CTR data in these initial stages of oxidation can also be successfully described by the stripe oxide alone. In region **II**, the growth of Pt_{ex2} does not saturate, contrary to that of Pt_{ex1}. As a result, oxidation at potentials higher than about 1.4 V primarily leads to a growth of the amorphous oxide phase.

To support the results obtained from the in situ HESXRD experiments, we performed DFT calculations on the oxide structure. Support for the stripe oxide phase was already found in our previous study.[23] Its formation was calculated to be favorable at ≥ 0.98 V, in good agreement with the experimental results. In our further analysis we focused on the onset of the second oxide's phase formation. Our starting point is a Pt stripe oxide with a coverage of 1/3 ML close to the onset of region **II** at 1.09 V, when the surface has an oxygen coverage of 1 ML, according to the surface Pourbaix diagram.[23] Under these conditions, all O species are located on top of the surface; the presence of subsurface oxygen was found to be energetically unfavorable.[23]

We assessed the formation of different types of extracted Pt atoms adjacent to the stripe oxide, which corresponds to the initial stage of the Pt_{ex2} formation. Figure 3 condenses the five reactions we considered. Reaction 1 is the extraction of a Pt atom from a row adjacent to the Pt_{ex1} stripe. This reaction is highly endothermic (1.26 eV), suggesting that Pt stripes may not form next to each other. Reaction 2 is the deposition of Pt^{2+} from the solution so as to form a Pt_{ex2} adatom on Pt(100). Again, this reaction is highly endothermic (1.90 eV) and suggests that depositing Pt^{2+} is unlikely at 1.09 V. However, depositing $PtOH^+$ appears to be energetically favorable, judging by the free energy of reaction 3 (−0.31 eV). Besides, adding a second Pt_{ex2}–OH moiety is still energetically favorable (−0.07 eV). Reaction 5 shows that the interconversion between Pt^{2+} and $PtOH^+$ in solution is thermodynamically possible. Further oxidation of Pt_{ex2}–OH to Pt_{ex2}–O requires a free energy of 1.06 eV and thus is unlikely at 1.09 V. Hence, our calculations indicate that the Pt_{ex2} species near the onset of region **II** are *PtOH moieties deposited next to the preexisting stripes. Increasing

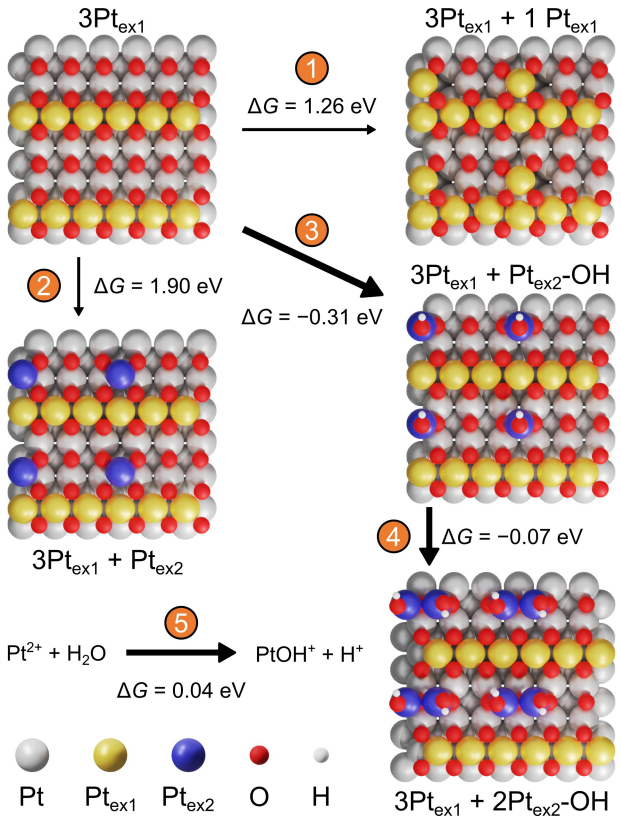

Figure 3. Mechanism of amorphous Pt_{ex2} formation. Top views of extraction processes starting from the formation of the Pt_{ex1} stripe at 1.09 V. Reaction 1 is the formation of an adjacent row of Pt_{ex1}. Reaction 2 is the formation of Pt_{ex2} from the deposition of Pt^{2+}. Reaction 3 is the formation of Pt_{ex2} from the deposition of $PtOH^+$. Reaction 4 is the formation of a second Pt_{ex2} from the deposition of $PtOH^+$. Reaction 5 is the transformation in solution of Pt^{2+} into $PtOH^+$. The free energies of the reactions are provided in each case. See Figure S10 for side views of the extraction processes.

deprotonation of the OH groups is expected at higher oxygen chemical potential, i.e., towards more positive potentials, but this was not addressed explicitly in the calculations performed here.

According to the DFT results, Pt_{ex1} and Pt_{ex2} are geometrically different: First, Pt_{ex1} forms square-planar complexes with oxygen atoms ($3Pt_{ex1}$ in Figure 3), whereas Pt_{ex2} is initially coordinated to two oxygen atoms underneath and one OH group above ($3Pt_{ex1}+Pt_{ex2}-OH$ in Figure 3). When the oxide grows ($3Pt_{ex1}+2Pt_{ex2}-OH$ in Figure 3), two Pt_{ex2} atoms are coordinated to three oxygen underneath and two OH groups above, and there is a Pt–Pt bond between them. Second, Pt_{ex1} and Pt_{ex2} are located at different heights with respect to the surface plane (see Figure S8): Pt_{ex1} is initially located at a height of 1.49 Å, which increases to 1.56 Å when two Pt_{ex2} are formed. On the other hand, the first Pt_{ex2} is at a height of 2.80 Å, which increases to 2.98 Å when the second Pt_{ex2} is added. Considering that no explicit water molecules were taken into account in the DFT calculations and that the calculations were restricted to the very initial stages of Pt_{ex2} formation, these positions are in reasonable agreement with the experimental results obtained from the CTR analysis. At higher potentials, further deprotonation of the PtOH moieties as well as the possible formation of subsurface oxygen will alter the local arrangement of oxygen around the Pt_{ex2} atoms and might change the in-plane location of Pt_{ex2}. However, we emphasize that high O coverage structures (>1 ML O) and potentials beyond 1.09 V were not addressed in the DFT calculations.

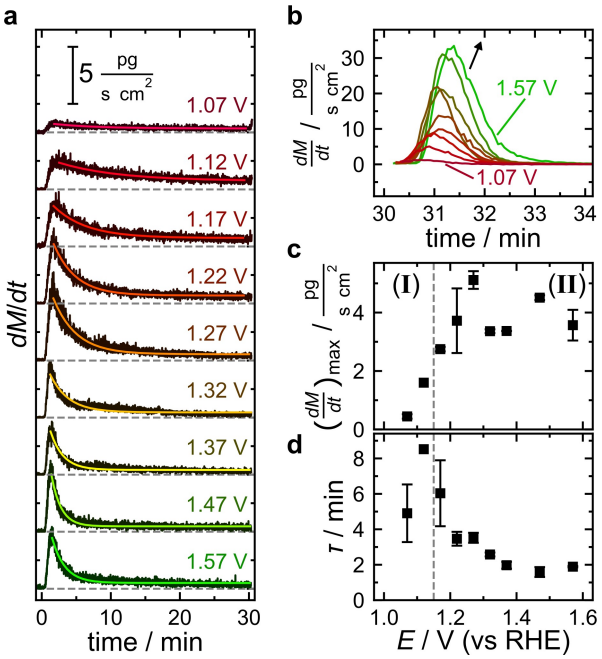

Figure 4. Pt dissolution during oxide formation and reduction. a) Anodic dissolution rate during a potential sweep with 50 mV/s from 0.17 V up to values between 1.07 and 1.57 V, where the potential was subsequently held for 30 minutes. Colored lines are fits by an exponential decay function. The dissolution profiles are offset from each other by 5 pg s^{-1} cm^{-2}. b) Cathodic dissolution rates during the reverse sweep to 0.17 V, obtained in the same experiments directly after the data in a). c) Amplitude $(dM/dt)_{max}$ and d) time constant τ of the exponential decay of the anodic dissolution. The error bars in c) and d) represent the standard deviation of 2 or 3 repetitions of the experiment (see the Supporting Information).

Correlation of oxide species with Pt dissolution and surface restructuring

To assess the influence of the surface oxide structure on Pt dissolution, we measured the rate of Pt dissolution during oxide formation and reduction in 0.1 M $HClO_4$ at 9 different potentials in between 1.07 V and 1.57 V with a scanning flow cell (SFC) and an inductively coupled plasma mass spectrometer (ICP-MS) setup. In each experiment, the oxide was formed on a freshly prepared Pt(100) sample during a linear potential sweep with 50 mV/s from 0.17 V to the respective upper potential, followed by a potential hold period of 30 min. Subsequently, the oxide was reduced with a second potential sweep with 50 mV/s down to 0.17 V. The measured dissolution rates during Pt oxidation (anodic dissolution) and Pt oxide reduction (cathodic dissolution) are shown in Figure 4a and b, respectively. Cathodic dissolution occurs in a single peak, which continuously increases towards more positive holding potentials. The anodic dissolution rates exhibit a peak shortly after reaching the holding potential followed by a slow decay. While this overall behavior is similar at all holding potentials, the detailed dissolution kinetics exhibits some interesting potential-dependent trends. To quantify these trends, the anodic dissolution profiles were fitted with an empirically chosen exponential decay function (see the Supporting Information for further details on the analysis of the dissolution profiles). First, the initial dissolution rate at $t=0$ min, determined from the amplitude $(dM/dt)_{max}$ of the exponential fits, increases up to 1.27 V and then saturates at a slightly lower level (Figure 4c). Second, the characteristic time constant (Figure 4d) initially increases to a maximum value of 8.2 min at 1.12 V and then gradually decreases to values around 2 min (the latter may be limited by the finite time resolution of the ICP-MS setup). Obviously, Pt dissolution during the initial stages of oxidation substantially differs from that found at potentials deep inside the Pt oxidation regime, a point which we will discuss in more detail below.

The dissolution rates in the cathodic peaks and in the anodic transients were integrated to obtain the total amount of anodic and cathodic dissolution shown in Figure 5a. To strictly correlate the observed dissolution behavior with the surface oxide phases, additional CTR measurements in 0.1 M $HClO_4$ were performed. In contrast to the measurements shown in Figure 2, where the potential was continuously increased in small steps, each of the experiments in Figure 5 started with a pristine Pt(100) sample and employed the identical potential program as the dissolution measurements, except for a longer potential hold period at the upper potential limit of about 45 minutes. As in the HESXRD measurements above, the CTR measurements were started five minutes after the upper potential was reached. Good CTR fits with the same surface oxide model

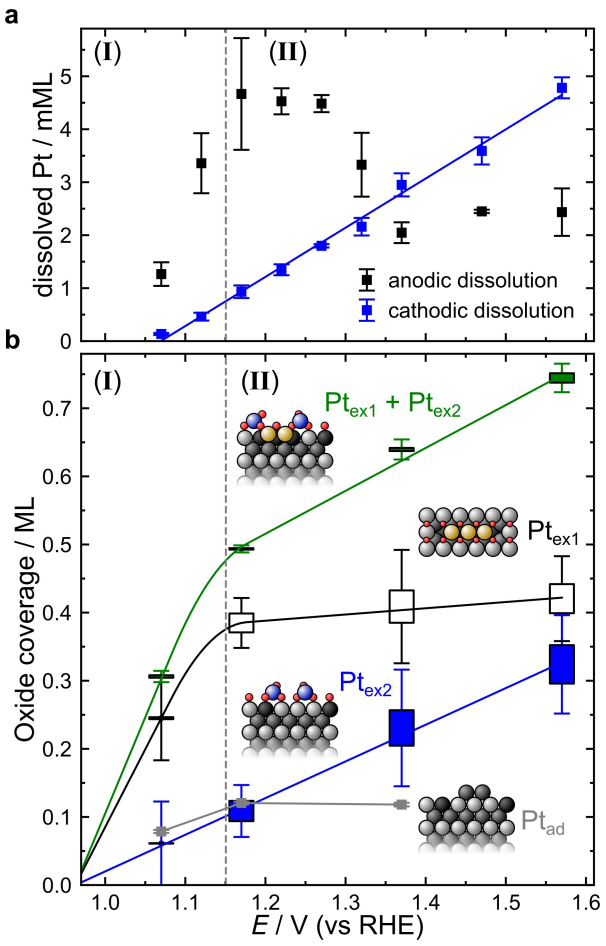

Figure 5. Correlation of anodic and cathodic Pt dissolution with Pt_{ex1} and Pt_{ex2} surface oxide species. a) Total amount of dissolved Pt during anodic and cathodic dissolution, obtained from the data shown in Figure 4a and 4b. b) Coverage of the two Pt surface oxide species Pt_{ex1} and Pt_{ex2} obtained from CTR measurements under identical conditions (see Figure S6). In addition, the total amount of Pt in the oxide, $Pt_{ex1} + Pt_{ex2}$, and the fraction of Pt adatoms after subsequent oxide reduction is shown. Rectangular boxes indicate the systematic error caused by the ambiguity of the location of the O_{ad} layer. The error bars represent the standard uncertainties of the CTR fits as standard deviations. Further details on the error analysis are given in Supporting Information.

as for the HESXRD data discussed in the previous paragraph with the two specific Pt oxide sites Pt_{ex1} and Pt_{ex2} were possible and yielded similar structural parameter values (Table S3 and Figure S6). The coverages of the Pt atoms in the stripe Pt_{ex1} and in the amorphous oxide Pt_{ex2} obtained from the CTR fits are shown in Figure 5b. These show a similar potential dependence as the data in Figure 2c, apart from an earlier saturation of the Pt_{ex1} coverage at about 0.4 ML at 1.17 V, followed by a lower Pt_{ex1} growth rate in region **II**. The latter is likely due to the differences in the potential program or the different electrolyte.

The total amount of cathodic dissolution increases linearly with potential. A similar linear increase is found for Pt_{ex2} coverage in the amorphous oxide (see Figure S11 for a correlation plot), whereas the Pt_{ex1} coverage as well as the total amount of Pt surface oxide ($Pt_{ex1} + Pt_{ex2}$) exhibits a clearly non-linear potential dependence. Dissolution from remaining patches of metallic platinum also cannot explain the linear increase of the cathodic dissolution since already at about 1.17 V the complete surface is covered by oxide (total coverage ca. 0.5 ML). Hence, the Pt_{ex2} in the amorphous oxide must be the platinum species that leads to dissolution during oxide reduction.

The total amount of anodic dissolution increases until 1.17 V, which correlates well with region **I**, where the initial stripe oxide is formed, and reaches a maximum at the crossover to region **II**. At more positive potentials, it decreases again and levels at a potential-independent value. A similar dependence of the amount of dissolved Pt on potential was also observed in the total amount of dissolution of polycrystalline platinum and of Pt nanoparticles[53–55] after potential holding for 72 hours. The observed potential dependence of the amount of dissolution was assigned to the equilibrium concentration of Pt in solution. However, contrary to those studies, our measurements were performed in a flow cell, which should eliminate the dissolution dependence on Pt^{2+} concentration in the electrolyte solution. According to the kinetic data in Figure 4c and 4d, the initial anodic dissolution rate, i.e., $(dM/dt)_{max}$, increases in region **I** and then remains approximately constant in region **II**. Subsequently, the dissolution rate decays only slowly in region **I**, whereas in region **II** the decay becomes gradually faster. This accounts for the maximum in the total amount of anodically dissolved Pt around 1.2 V.

The above described dissolution behavior can be explained on the basis of our previous work, where we showed by DFT that growth of the stripe oxide phase leads to Pt dissolution above 0.98 V.[23] Specifically, the excess Pt atoms that are displaced onto the surface at the end of the stripes were found to be unstable against dissolution. According to the results presented here, the coverage of the surface with oxide stripes increases with potential in region **I** and thus the initial dissolution rate $(dM/dt)_{max}$ increases. At the crossover to region **II**, the entire surface is covered with stripes and $(dM/dt)_{max}$ saturates. The decay of the Pt dissolution rate for potential holds in region **II** may result from the emergence of a competing process that consumes the Pt atoms at the stripe ends, making them less available for dissolution. Such a competing process could be the transformation of these Pt atoms into Pt_{ex2}, which are bound to the surface in the form of the amorphous oxide.

We note that even after 30 minutes anodic dissolution is observed at all potentials, albeit at very low rate (see Figure 4a). This may suggest that slow chemical dissolution of the Pt oxide can occur even after all weakly-bound Pt atoms at stripe ends are dissolved or transformed into Pt_{ex2}. However, the presence of long-term steady-state dissolution is difficult to confirm experimentally, because of limited long-term stability in the ICP-MS measurements. From an application point of view, this question is less relevant, because the cathode potential in fuel cells is usually controlled in a way that the electrode potential is only for

short time periods in the potential range >1 V, where significant Pt oxidation occurs.

Our observations indicate that Pt_{ex2} in the amorphous oxide is stable against dissolution at potentials ≥1.1 V but can be readily dissolved during the cathodic reduction of the Pt oxide. This is not surprising, considering that the Pt_{ex2} species likely is in a similar oxidation state as in PtO_2 (see above). According to thermodynamic considerations, PtO_2 is stable above 1.045 V under acidic conditions, whereas it dissolves at potentials in the range of oxide reduction.[4] A similar reaction pathway for cathodic Pt dissolution mechanism was derived from DFT calculations by Duan and Henkelman for the case of Pt(111).[24] In that study it was proposed that platinum atoms in the oxide, which are coordinated with four oxygen atoms, are sequentially reduced to a hydroxide, which is subsequently dissolved. Our DFT calculations indicate that the Pt_{ex2} correspond to a species, which is only weakly coordinated to the Pt(100) metal surface via surface oxygen species and OH terminated. Upon reduction of Pt_{ex2} the terminal OH groups may leave in form of H_2O, in which case the reverse of reaction 2 in Figure 3 can take place, which is highly exothermic and leads to Pt dissolution. Thus, the presence of a similar dissolution mechanism as proposed by Duan and Henkelman seems likely.

From the literature it is clear that the Pt(111) surface undergoes similar structural transformation from a surface-embedded and potentially stripe-like oxide[56–59] to a more disordered, amorphous oxide.[27,29] Furthermore, the anodic and cathodic Pt dissolution amounts exhibit similar potential-dependent trends on all low-index planes,[22,25] which may indicate a similar dissolution mechanism as proposed here for Pt(100). More detailed potential-dependent studies of anodic[53–55] and cathodic dissolution[17] of polycrystalline surfaces and carbon-supported nanoparticles (see also Ref. [4] and references therein) reveal a potential dependence that is in good qualitative agreement with our data on Pt(100) (Figure 5a), suggesting also for these more realistic catalysts a mechanism involving two different surface oxide species.[30,31] However, potential-dependent surface structural and dissolution data that can be clearly correlated, as done in the present study, were not reported in these previous studies.

Finally, we also address briefly the surface roughening induced by a surface oxidation/reduction cycle. This was assessed by determining the coverage of Pt atoms in lattice sites on top of the surface layer (Pt_{ad}) and the corresponding coverage of vacancies after reduction of the surface oxides, which were characterized in the previous paragraph. The coverage of the Pt_{ad} is shown together with the coverages of the Pt_{ex1} and Pt_{ex2} in the corresponding oxide in Figure 5. The values for Pt_{ad} were obtained from fits of the CTRs measured after a potential sweep to 0.17 V (see Figure S7 for the full CTR data sets). Here, platinum loss due to dissolution was neglected as the obtained adatom coverage was 20–100 times higher than the amount of dissolution during oxidation and reduction. Furthermore, the formation of three-dimensional adislands is only expected after multiple oxidation and reduction cycles[21,35–37,59,60] and can therefore also be neglected. In region **I** and the crossover to region **II**, the Pt_{ad} coverage equals that of the Pt_{ex2} species. This observation is in good agreement with our previous work, where we concluded that the surface roughening of Pt(100) in the initial stages of oxidation is caused by the detachment of the unstable platinum atoms from the ends of the oxide stripes and their subsequent reduction to metallic Pt adatoms.[23] Here, our results suggest that these detached Pt atoms are not bound as metallic adatoms on the oxidized surface, but instead are incorporated into the amorphous oxide as Pt_{ex2}. Upon reduction, the Pt_{ex1} within the oxide stripes can easily return into the adjacent vacancy sites underneath. In contrast, Pt_{ex2} recombination with a vacancy site requires long range mass transport, which is impeded by the low Pt surface mobility on Pt(100). Studies under UHV conditions revealed Pt_{ad} diffusion barriers >0.5 eV on the positively charged Pt(100) surface[61] as well as a significant inhibition of Pt_{ad} surface diffusion by coadsorbed species such as hydrogen.[62] In the presence of adsorbed O or OH species, similar or even stronger blocking of Pt surface diffusion seems likely. In addition, Pt_{ad} recombination with vacancies requires overcoming an additional barrier, similar to the Ehrlich-Schwoebel barrier for diffusion across steps, and thus is further hindered. Because of these effects, little recombination is expected to occur in region **I**, where the oxide consists of isolated oxide stripes and the Pt_{ad} and the corresponding vacancy can form at different positions along the stripe on an otherwise smooth Pt(100) surface. In contrast, the oxide formed in region **II** fully covers the Pt surface, resulting in a strongly distorted surface layer with a high surface density of vacancy and adatom sites. Here, only short range mass transport is required and recombination is facilitated, which explains why the Pt_{ad} saturates at a potential-independent value of about 0.1 ML.

Conclusion

The combined in situ HESXRD, DFT, and ICP-MS results presented in this work provide a detailed atomic-scale picture of electrochemical Pt(100) oxidation, from its onset up to potentials as high as 1.6 V, as well as its influence on Pt dissolution and Pt oxide reduction. We have shown that the oxidation starts near 1.0 V with the formation of an oxide phase that is commensurate to the underlying metal lattice, into which the extracted Pt atoms are still partly embedded. At a latter stage, above about 1.1 V, formation of a second (hydr)oxide phase commences, in which the Pt ions are located further away from the Pt surface and more loosely coordinated to it. These two surface oxide phases evolve in parallel over a wide potential range (limited by the inherent restriction of the commensurate Pt oxide to a coverage of 0.5 ML). Most interestingly, they affect the stability of the Pt surface against dissolution in a different way. While nucleation and growth of the commensurate stripe-like oxide plays a major role in the Pt dissolution during oxide formation, the dissolution observed during Pt oxide reduction predominantly occurs from the second, more disordered (hydr-)oxide phase. Consequently, the

former process dominates the dissolution behavior at potentials <1.3 V, the latter the behavior at higher potentials, reflecting the potential-dependent coverages of the two oxide phases.

While the importance of dynamic oxide formation and reduction for Pt dissolution was already found in previous studies, our results enable an explanation of these phenomena in a detailed atomistic picture. Specifically, they enable linking the dissolution mechanisms to the precise structures of the involved surface oxide phases, which differ distinctly from those of bulk Pt oxides. Our results point to specific elementary steps during the dynamic structural changes that are most relevant for the electrode's stability against dissolution and restructuring. If these steps can be blocked or be made energetically less favorable by optimized system design, the catalyst stability can be increased. Such fundamental insights into the oxidation and dissolution mechanism are an important step towards knowledge-based strategies for designing and developing more stable fuel cells. Concretely, precise knowledge on the degradation pathways may help in the targeted design of tailored nanocatalysts where these pathways are suppressed. A prerequisite for this is the development of predictive capabilities based on ab initio calculations. Our studies of catalyst degradation in structurally well-defined model systems provide a testbed for the development of such approaches.

Acknowledgements

The SXRD experiments were performed on beamlines ID31 and ID03 at the European Synchrotron Radiation Facility (ESRF), Grenoble, France. We are grateful to F. Carlà, H. Isern and T. Dufrane at the ESRF for providing assistance in using the beamline ID03 and H. Isern for providing assistance in using the beamline ID31. Funding is acknowledged from Deutsche Forschungsgemeinschaft for OMM and SC (project number 418603497), for OMM by the German Federal Ministry of Education and Research (BMBF) via project 05K19FK3, and for DAH by the NSERC (grant RGPIN-2017-04045). FCV acknowledges that the grants PID2021-127957NB-I00 and TED2021-132550B-C21 were funded by MCIN/AEI/ 10.13039/ 501100011033 and by the European Union. The use of supercomputing facilities at SURFsara was sponsored by NWO Physical Sciences, with financial support by NWO. Open Access funding enabled and organized by Projekt DEAL.

Conflict of Interest

The authors declare no competing interests.

Data Availability Statement

The data that support the findings of this study are available from the corresponding author upon reasonable request.

Keywords: catalyst degradation · density functional calculations · online mass spectrometry · platinum oxidation · X-ray diffraction

[1] T. Zhang, P. Wang, H. Chen, P. Pei, *Appl. Energy* **2018**, *223*, 249.
[2] B. G. Pollet, S. S. Kocha, I. Staffell, *Curr. Opin. Electrochem.* **2019**, *16*, 90.
[3] J. C. Meier, C. Galeano, I. Katsounaros, J. Witte, H. J. Hongard, A. A. Topalov, C. Haldizzone, S. Mezzavilla, F. Schüth, K. J. J. Mayrhofer, *Beilstein J. Nanotechnol.* **2014**, *5*, 44.
[4] S. Cherevko, N. Kulyk, K. J. Mayrhofer, *Nano Energy* **2016**, *29*, 275.
[5] A. A. Topalov, I. Katsounaros, M. Auinger, S. Cherevko, J. C. Meier, S. O. Klemm, K. J. Mayrhofer, *Angew. Chem. Int. Ed.* **2012**, *51*, 12613.
[6] C. A. Heiser, L. Hregoli, T. W. Patterson, J. S. Yi, J. D. Yang, M. L. Perry, T. D. Jarvi, *Electrochem. Solid-State Lett.* **2005**, *8*, A273.
[7] H. Tang, Z. Qi, M. Hamani, J. F. Elter, *J. Power Sources* **2006**, *158*, 1306.
[8] L. Xing, G. Jerkiewicz, D. Heauchemin, *Anal. Chim. Acta* **2013**, *785*, 16.
[9] L. Xing, M. A. Hossain, M. Tian, D. Heauchemin, K. T. Adjemian, G. Jerkiewicz, *Electrocatalysis* **2014**, *5*, 96.
[10] M. Umeda, Y. Okuda, S. Takizawa, M. Inoue, A. Nakazawa, *Electrocatalysis* **2018**, *9*, 243.
[11] Z. Wang, E. Tada, A. Nishikata, *J. Electrochem. Soc.* **2014**, *161*, F380.
[12] J. Schröder, H. K. Pittkowski, I. Martens, H. Chattot, J. Drnec, J. Quinson, J. J. K. Kirkensgaard, M. Arenz, *ACS Catal.* **2022**, *12*, 2077.
[13] I. Martens, H. Chattot, M. Hasola, M. V. Hlanco, V. Honkimäki, D. Hizzotto, D. P. Wilkinson, J. Drnec, *ACS Appl. Energ. Mater.* **2019**, *2*, 7772.
[14] I. Martens, H. Chattot, J. Drnec, *J. Power Sources* **2022**, *521*, 230851.
[15] P. P. Lopes, D. Tripkovic, P. F. Martins, D. Strmcnik, E. A. Ticianelli, V. H. Stamenkovic, N. M. Markovic, *J. Electroanal. Chem.* **2018**, *819*, 123.
[16] J. Cho, H. Kim, H.-s. Oh, C. H. Choi, *JACS Au* **2023**, *3*, 105.
[17] A. A. Topalov, S. Cherevko, A. H. Zeradjanin, J. C. Meier, I. Katsounaros, K. J. J. Mayrhofer, *Chem. Sci.* **2014**, *5*, 631.
[18] H. E. Conway, G. Jerkiewicz, *J. Electroanal. Chem.* **1992**, *339*, 123.
[19] H. You, D. J. Zurawski, Z. Nagy, H. M. Yonco, *J. Chem. Phys.* **1994**, *100*, 4699.
[20] P. P. Lopes, D. Strmcnik, D. Tripkovic, J. G. Connell, V. Stamenkovic, N. M. Markovic, *ACS Catal.* **2016**, *6*, 2536.
[21] N. Arulmozhi, D. Esau, H. P. Lamsal, D. Heauchemin, G. Jerkiewicz, *ACS Catal.* **2018**, *8*, 6426.
[22] D. J. S. Sandbeck, O. Hrummel, K. J. J. Mayrhofer, J. Libuda, I. Katsounaros, S. Cherevko, *ChemPhysChem* **2019**, *20*, 2997.
[23] T. Fuchs, J. Drnec, F. Calle-Vallejo, N. Stubb, D. J. S. Sandbeck, M. Ruge, S. Cherevko, D. A. Harrington, O. M. Magnussen, *Nat. Catal.* **2020**, *3*, 754.
[24] Z. Duan, G. Henkelman, *ACS Catal.* **2021**, *11*, 14439.
[25] V. Komanicky, K. C. Chang, A. Menzel, N. M. Markovic, H. You, X. Wang, D. Myers, *J. Electrochem. Soc.* **2006**, *153*, H446.

[26] J. Drnec, M. Ruge, F. Heikowski, B. Rahn, F. Carla, H. Felici, J. Stettner, O. M. Magnussen, D. A. Harrington, *Electrochim. Acta* **2017**, *224*, 220.
[27] L. Jacobse, V. Vonk, I. T. McCrum, C. Seitz, M. T. Koper, M. J. Rost, A. Stierle, *Electrochim. Acta* **2022**, *407*, 13988l.
[28] M. J. Eslamibidgoli, M. H. Eikerling, *Electrocatalysis* **2016**, *7*, 345.
[29] M. Ruge, J. Drnec, B. Rahn, F. Heikowski, D. A. Harrington, F. Carla, H. Felici, J. Stettner, O. M. Magnussen, *J. Electrochem. Soc.* **2017**, *164*, H608.
[30] H. Mom, L. Frevel, J.-J. Velasco-Velez, M. Plodinec, A. Knop-Gericke, H. Schlögl, *J. Am. Chem. Soc.* **2019**, *141*, 6537.
[31] Y. Takagi, H. Wang, Y. Uemura, T. Nakamura, L. Yu, O. Sekizawa, T. Uruga, M. Tada, G. Samjeske, Y. Iwasawa, T. Yokoyama, *Phys. Chem. Chem. Phys.* **2017**, *19*, 6013.
[32] J. Hammond, N. Winograd, *J. Electroanal. Chem. Interfacial Electrochem.* **1977**, *78*, 55.
[33] Y.-F. Huang, P. J. Kooyman, M. T. M. Koper, *Nat. Commun.* **2016**, *7*, 12440.
[34] J. Gustafson, M. Shipilin, C. Zhang, A. Stierle, U. Hejral, U. Huett, O. Gutowski, P. A. Carlsson, M. Skoglundh, E. Lundgren, *Science* **2014**, *343*, 758.
[35] N. Furuya, M. Ichinose, M. Shibata, *J. Electroanal. Chem.* **1999**, *460*, 251.
[36] N. Furuya, M. Shibata, *J. Electroanal. Chem.* **1999**, *467*, 85.
[37] L. Jacobse, Y.-F. Huang, M. T. M. Koper, M. J. Rost, *Nat. Mater.* **2018**, *17*, 277.
[38] Z. Nagy, H. You, *Electrochim. Acta* **2002**, *47*, 3037.
[39] Y. Liu, A. Harbour, V. Komanicky, H. You, *J. Phys. Chem. C* **2016**, *120*, 16174.
[40] A. Rodes, M. Zamakhchari, K. El Achi, J. Clavilier, *J. Electroanal. Chem. Interfacial Electrochem.* **1991**, *305*, 115.
[41] L. Kibler, A. Cuesta, M. Kleinert, D. Kolb, *J. Electroanal. Chem.* **2000**, *484*, 73.
[42] G. A. Attard, A. Hrew, K. Hunter, J. Sharman, E. Wright, *Phys. Chem. Chem. Phys.* **2014**, *16*, 3689.
[43] R. Rizo, E. Herrero, V. Climent, J. M. Feliu, *Curr. Opin. Electrochem.* **2023**, *38*, 101240.
[44] F. Sugimura, N. Sakai, T. Nakamura, M. Nakamura, K. Ikeda, T. Sakai, N. Hoshi, *Phys. Chem. Chem. Phys.* **2017**, *19*, 2757.
[45] H. E. Conway, H. Harnett, H. Angerstein-Kozlowska, H. V. Tilak, *J. Chem. Phys.* **1990**, *93*, 8361.
[46] T. Fuchs, V. Hriega-Martos, J. O. Fehrs, C. Qiu, M. Mirolo, C. Yuan, S. Cherevko, J. Drnec, O. M. Magnussen, D. A. Harrington, *J. Phys. Chem. Lett.* **2023**, *14*, 3589.
[47] Y. Furuya, T. Mashio, A. Ohma, M. Tian, F. Kaveh, D. Heauchemin, G. Jerkiewicz, *ACS Catal.* **2015**, *5*, 2605.
[48] L. Strandberg, V. Shokhen, M. Luneau, G. Lindbergh, C. Lagergren, H. Wickman, *ChemElectroChem* **2022**, *9*.
[49] C. Ellinger, A. Stierle, I. K. Hobinson, A. Nefedov, H. Dosch, *J. Phys. Condens. Matter* **2008**, *20*, 184013.
[50] S. A. Krasnikov, S. Murphy, N. Herdunov, A. P. Mc-Coy, K. Hadican, I. V. Shvets, *Nanotechnology* **2010**, *21*, 335301.
[51] J. R. McBride, G. W. Graham, C. H. Peters, W. H. Weber, *J. Appl. Phys.* **1991**, *69*, 1596.
[52] N. Seriani, W. Pompe, L. C. Ciacchi, *J. Phys. Chem. B* **2006**, *110*, 14860.
[53] X. Wang, H. Kumar, D. J. Myers, *Electrochem. Solid-State Lett.* **2006**, *9*, A225.
[54] H. K. Ahluwalia, S. Arisetty, J.-K. Peng, H. Subbaraman, X. Wang, N. Kariuki, D. J. Myers, H. Mukundan, H. Horup, O. Polevaya, *J. Electrochem. Soc.* **2014**, *161*, F291.
[55] D. J. Myers, X. Wang, M. C. Smith, K. L. More, *J. Electrochem. Soc.* **2018**, *165*, F3178.
[56] S. P. Devarajan, J. A. Hinojosa, J. F. Weaver, *Surf. Sci.* **2008**, *602*, 3116.
[57] M. A. van Spronsen, J. W. M. Frenken, I. M. N. Groot, *Nat. Commun.* **2017**, *8*, 429.
[58] S. Hanselman, I. T. McCrum, M. J. Rost, M. T. M. Koper, *Phys. Chem. Chem. Phys.* **2020**, *22*, 10634.
[59] M. J. Rost, L. Jacobse, M. T. M. Koper, *Angew. Chem. Int. Ed.* **2023**, e202216376.
[60] M. Ruge, J. Drnec, B. Rahn, F. Heikowski, D. A. Harrington, F. Carla, H. Felici, J. Stettner, O. M. Magnussen, *J. Am. Chem. Soc.* **2017**, *139*, 4532.
[61] G. L. Kellogg, *Phys. Rev. Lett.* **1993**, *70*, 1631.
[62] G. L. Kellogg, *Phys. Rev. Lett.* **1997**, *79*, 4417.

Manuscript received: March 24, 2023
Accepted manuscript online: June 21, 2023
Version of record online: July 14, 2023